Microstructural Origin of the Skeletal Ferrite Morphology of Austenitic Stainless Steel Welds

J. A. BROOKS, J. C. WILLIAMS, and A. W. THOMPSON

Scanning transmission electron microscopy (STEM) was conducted on welds exhibiting a variety of skeletal, or vermicular ferrite morphologies in addition to one lathy ferrite morphology. These ferrite morphologies result from primary ferrite solidification followed by a solid state transformation upon cooling. During cooling, a large fraction of the ferrite transforms to austenite leaving a variety of ferrite morphologies. Comparison of composition profiles and alloy partitioning showed both the skeletal and lathy ferrite structures result from a diffusion controlled solid state transformation. However, the overall measured composition profiles of the weld structure are a result of partitioning during both solidification and the subsequent solid state transformation.

I. INTRODUCTION

CONSIDERABLE attention has recently been given to the evolution of microstructures common to austenitic stainless steel welds. Weld ferrite content of the commercial AISI 300 series alloys typically varies from none to ~20 volume percent depending mainly upon alloy composition, and to a lesser extent upon weld cooling rate.[1-5] Several studies have characterized the variety of ferrite morphologies which are commonly observed.[6-9]

Interpretation of the formation of the different ferrite morphologies is complicated by the nonequilibrium conditions associated with welding. These conditions are further complicated by the solid state transformation during cooling, as evident from the 70 pct constant Fe vertical section of the Fe-Ni-Cr ternary diagram shown in Figure 1. The equilibrium phase of composition C_0 plotted on this diagram is ferrite at high temperatures and austenite at low temperatures. This composition passes through the $\delta + \gamma$ two phase region upon cooling. The microstructures resulting from the phase change have been related to the arrangement of the phase diagram[7] and to the Cr_{eq}/Ni_{eq} ratio[4] but are also affected by cooling rate.[7,8,10] However, due to segregation during solidification, welds of the alloy of nominal composition C_0 can be expected to contain a range of compositions prior to any solid state transformation, further complicating the microstructural interpretation. Thus, in discussing the nature of the solid state transformations, the solidification sequence must also be considered.

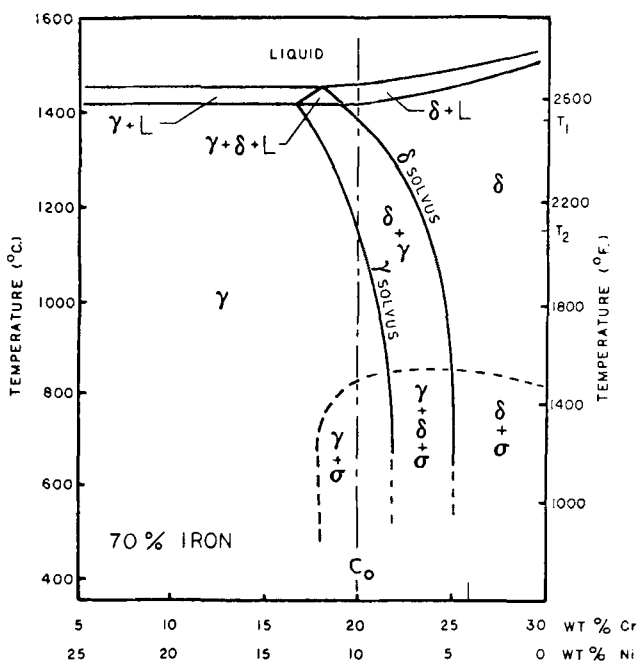

Fig. 1—The 70 pct constant Fe vertical section of the Fe-Ni-Cr system.

The composition profiles in castings and welds resulting from solidification are obviously related to the nature of the constitutional diagrams. Davies[11] schematically summarized the composition profiles in the solid predicted by different models as shown in Figure 2 for the case in which the equilibrium distribution coefficient $k < 1$. The fraction of melt of initial composition C_0 which has solidified is plotted along the abscissa. In the case of welds solidifying in a columnar dendritic mode, the solid starts to form at the

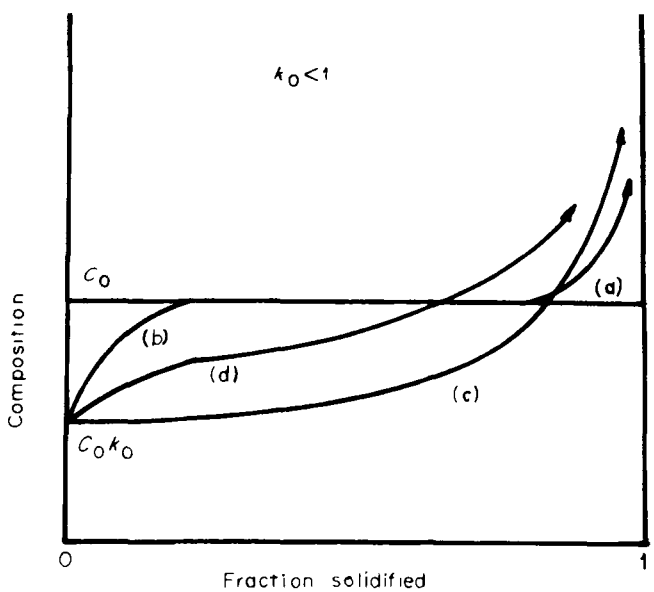

Fig. 2—Solute distributions predicted by different models in a frozen bar from liquid of composition C_0: (*a*) equilibrium freezing, (*b*) solute mixing in the liquid by diffusion only, (*c*) complete mixing in the liquid, and (*d*) partial solute mixing in the liquid. From Davies, Ref. 11.

J. A. BROOKS is Member, Technical Staff, Sandia National Laboratories, Livermore, CA 94550; J. C. WILLIAMS is President, Mellon Institute, Pittsburgh, PA 15213; and A. W. THOMPSON is Professor, Metallurgical Engineering and Materials Science Department, Carnegie-Mellon University, Pittsburgh, PA 15213.

Manuscript submitted May 11, 1982.

dendrite core, and the fraction of solid (f_s) approaches 1 in the interdendrite region during dendrite impingement. Several of the simple assumptions about solidification modes are presented below. It should be kept in mind that each of these can be only an approximation to actual welding; it has been observed that a variety of factors in welding may control the solute distribution and may also result in quite different concentration profiles.[12]

Curve (a) in Figure 2 shows the uniform composition profile C_0 for equilibrium solidification. The other three cases are for no diffusion in the solid, but equilibrium at the solid-liquid interface. The most common assumption used in the solidification of castings is that of complete mixing in the liquid, resulting in the well-known Scheil Eq. [13].

The composition profile given by this equation is shown as (c) in Figure 2. Note the final liquid solidifies at an invariant composition such as a eutectic. In welds, this then occurs within the intercellular or interdendritic regions.

The third case shown in Figure 2, curve (b), is for mixing in the liquid by diffusion only, which results in the formation of a solute-rich boundary layer at the solid-liquid interface. Solutions for condition (b) have been derived by Tiller *et al.*[14,15] Their equations predict an initial transient region until an equilibrium boundary layer is formed. The concentration profile in the resulting solid is shown as (b) in Figure 2. The distance over which the initial transient has risen to $1 - (1/e)$ of its maximum value for small k is $X_i = D_l/Vk$ where D_l is the diffusion coefficient in the liquid and V is the solidification velocity. The length of the final transient is smaller than the initial transient for small values of k and is given as D_l/V.[11]

The final case, (d), is for some mixing in the liquid by convection in addition to diffusion, which has been treated by Burton, Prim, and Slichter.[16] Their solution falls between that predicted by the Scheil Equation, curve (c), and the mixing by diffusion only case, curve (b), and is shown as curve (d) in Figure 2. In all cases summarized the initial solid to form at the dendrite core is of composition C_0k.

It is evident from the solidification models summarized in Figure 2 that a range in compositions can exist across the solidified structure. As can be determined by Figure 1, a large fraction of the melt can solidify as ferrite but subsequently transform to austenite upon cooling. Quenching experiments on small castings and welds have shown that as much as 75 to 80 pct of the liquid in nominal 304 compositions may solidify by primary ferrite before austenite also starts to form from the remaining melt.[19,20,21] Frederiksson[10] used controlled solidification experiments to study the development of the skeletal ferrite morphology. Alloy of 304 composition was contained in a thin-walled alumina tube and solidified in a steep temperature gradient furnace. When the partially-solidified samples were brine quenched, he found that the tip of the individual dendrites at the solidification front transformed to a lathy ferrite morphology. Farther down each dendrite where the cooling rate was much slower, the ferrite morphology was skeletal. From these experiments Frederiksson concluded that the skeletal ferrite resulted *via* a diffusion-controlled reaction with partitioning of Ni to the austenite and Cr to the ferrite, leaving only a Cr-rich, Ni-lean ferrite core along the dendrite center (*i.e.*, skeletal ferrite); this core becomes the stable ferrite at room temperature. Arata and co-workers observed similar behavior in welds.[19]

David *et al*[2] used 308 weld metal and Differential Thermal Analysis to study the solidification sequence. They concluded, as did Frederiksson, and has recently been shown schematically by Suutala *et al*,[6] that primary solidification occurred as ferrite; however, after partial solidification the ferrite is enveloped by austenite until solidification proceeds to completion. This solidification sequence is characteristic of a peritectic. These investigators also suggest that upon cooling, a large fraction of the primary ferrite is consumed by austenite in a diffusion-controlled solid state transformation. The different ferrite morphologies have been illustrated in a schematic diagram by Suutala *et al.*[6] A somewhat modified schematic of the solidification behavior and resulting ferrite morphologies of primary ferrite solidified welds is shown in Figure 3.

Lippold and Savage[7,17,18] related the formation of the skeletal ferrite morphology to the composition profiles resulting from solidification using the equations developed by Tiller *et al*[14,15] for mixing in the liquid by diffusion only. In Figure 4 are the profiles which they predict for primary ferrite solidification.[17] They suggest that the skeletal morphology is the result of a Cr-enriched, Ni-depleted dendrite core formed during the initial transient stage of solidification. This is the only retained ferrite, even though at the elevated temperature a large fraction of the dendrite is ferrite. They suggested that the transformation of the ferrite to austenite is "massive" in nature. A massive transformation occurs by the migration of a disordered interface and involves trans-interphase interface diffusion, but no long-range diffusion.[21] Thus, the massive product inherits the parent phase composition which in this case would be that established by the solidification mechanics.

They further suggest that the bulk of the dendrite at composition C_0, which solidifies as primary ferrite, is stable austenite at room temperature, and that the ferrite-austenite boundary originally near the cell boundary moves inward until it reaches a point at which the compositional driving force is insufficient for further boundary motion. This position is located somewhere within the initial transient region at the subgrain core shown schematically in Figure 4. They used an argument based on the $(4Dt)^{1/2}$ diffusion distance, and presented data for Cr and Ni diffusion in austenite[22,23] to suggest that the diffusion distances are too great for a diffusion-controlled transformation during the short times available in welds. They suggest that at cooling rates of ~550 °C per second and diffusion occurring only within the two-phase ferrite + austenite region of the equilibrium phase diagram, that the diffusion time is on the order of 0.2 seconds. The authors then employed both microprobe and STEM (scanning transmission electron microscopy) data from primary-ferrite-solidified structures to support this solidification model.[17,18] This controversy[7,10,17,18,21] as to the nature of the transformation resulting in skeletal ferrite is still unresolved in the literature. The purpose of this study was to investigate further the nature of the solid state transformation resulting in the final skeletal ferrite morphology in order to resolve unambiguously the process involved.

II. MATERIALS

Samples for this study were obtained from GTA welds of Fe-Ni-Cr ternary alloys and experimental heats of AISI 309

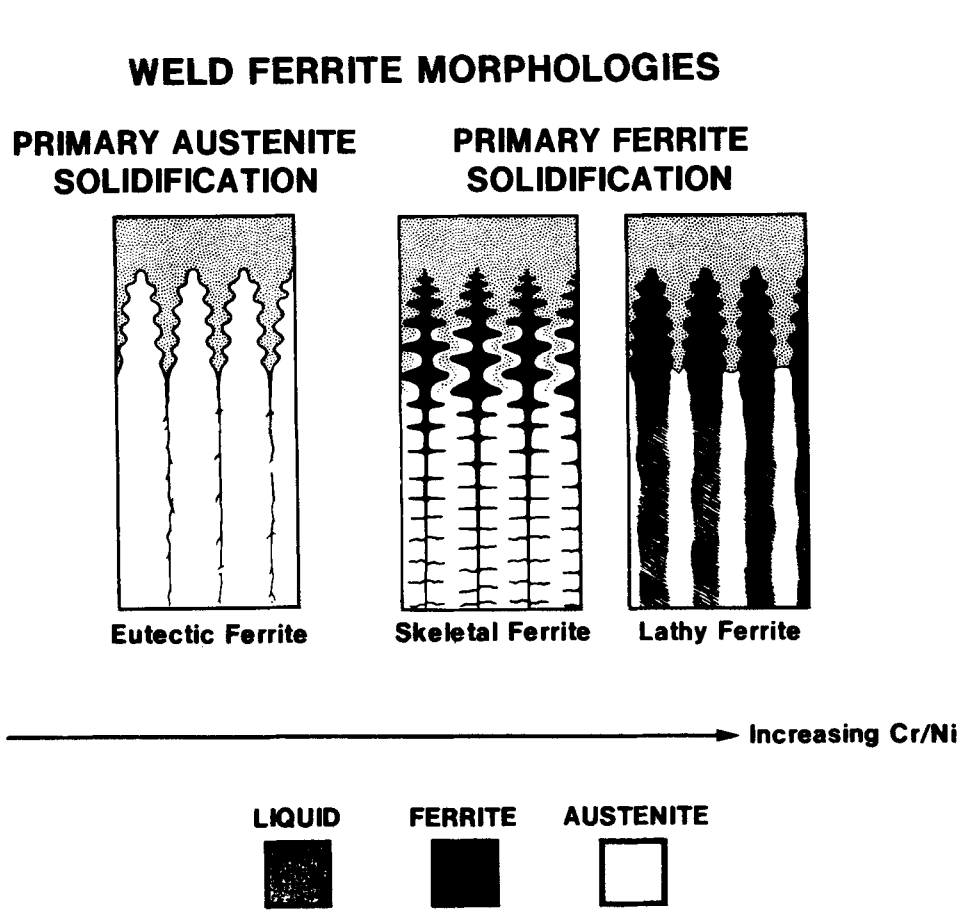

Fig. 3 — The solidification sequence and solid state transformations producing different ferrite morphologies of primary ferrite solidified welds.

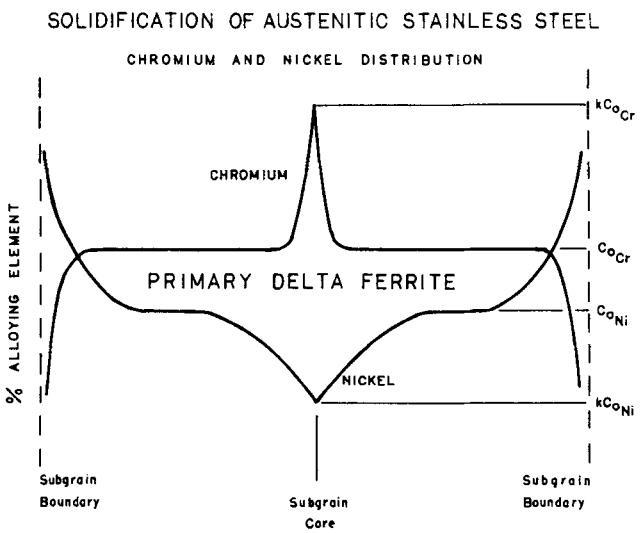

Fig. 4 — Composition profiles predicted by Lippold and Savage (Ref. 17) for primary ferrite solidification using equations of Smith, Tiller, and Rutter.[15]

stainless steel or from small castings of the ternary alloy. The ternary alloy was in the form of 9.5 mm thick "sheet bar" while the 309 alloys were in the form of 0.25 mm thick sheet. Autogenous welds were made at a speed of 10 mm per second on the 309 alloys and 1.8 mm per second on the ternary plates. Detailed sample preparation has been reported elsewhere.[9] The chemical compositions of the experimental alloys, all vacuum induction melted, are given in Table I. Note that the alloy designations of the ternary alloys correspond to the Cr and Ni concentrations.

III. STEM ANALYSIS TECHNIQUE

Micro-chemical analysis was conducted on a JEOL JEM 120CX STEM unit. The unit was equipped with an energy dispersive X-ray spectrometer which was interfaced with a KEVEX 700 μx data acquisition and reduction system. The Quantex-Ray program[24] uses the Cliff-Lorimer[25] technique to calculate the composition from the integrated intensities. A computer-generated background was subtracted from

Table I. Chemistries of Experimental Heats (Wt Pct)

Alloy	Cr	Ni	Mn	Si	C	N	P	S
1 (309)	22.0	13.7	1.50	0.71	0.06	0.02	0.058	0.031
2 (309)	25.1	14.0	1.56	0.73	0.05	0.02	0.048	0.044
22-13 (Ternary)	21.9	13.1	—	0.01	0.016	0.003	0.003	0.004
25-14 (Ternary)	25	14.2		0.01	0.006	0.001	0.003	0.002

*Balance Fe

the collected spectrum before the analysis was conducted. Typical counting times were 100 seconds. This resulted in standard deviation values of Cr and Ni ~0.15 to 0.2 wt pct obtained from the counting statistics. The data obtained were semi-quantitative in character. Of primary concern for this study is the nature of the concentration profile measured within the region analyzed. However, the analysis obtained on the ternary alloys was found to be in good agreement with that of the heat chemistry analysis, indicating reasonable absolute accuracy of the data.

In the analysis, the 309 weld specimens were treated as Fe-Ni-Cr ternaries, excluding Mn and Si. The computer-generated background worked very satisfactorily at the higher energy levels of the Fe, Ni, and Cr peaks. However, with elements of low atomic number the computer-generated background was not satisfactory, especially considering the low number of counts generated by Si. The resulting Si analysis was typically two to three times too high. When Mn is included in the analysis, the computation time increases considerably due to the overlap in the Cr K_β and Mn K_α peaks. However, since in the analysis the intensities of only the K_α peaks are considered, ignoring the presence of Mn will not interfere with the measured intensity ratios. Since the sum of (Mn + Si) is ~2 pct, the reported values of Cr and Ni of the 309 welds are likely ~2 pct high. No attempt was made to correct the data, since Mn and Si are expected to partition to some extent within ferrite and austenite. These problems did not arise with the ternary alloys.

The advantage of using STEM over more conventional microprobe techniques is the much improved spatial resolution achieved by using a thin foil and a higher accelerating voltage (100 kV). Although a spot (beam) size of <30 Å is possible with the instrument, a spot of ~100 Å was used to increase the count rate and hence improve the counting statistics for a given analysis time. Using the data of Goldstein,[26] the beam broadening can be expected to be ~300 Å for typical foil thicknesses used, ~1500 Å. Thus, for this foil thickness, the spatial resolution is ~400 Å.

When analysis was to be taken near a phase boundary the sample was scanned to find a region where the interface was most nearly parallel to the beam when the specimen was tilted at the 30 deg angle required for the X-rays to reach the detector. In this case, analysis can be taken much closer to the phase boundary before the beam spreads across it into the adjoining phase. In some cases when several boundaries were traversed it was not possible to find a region where all boundaries were parallel.

IV. LIGHT MICROSCOPY

Metallography was conducted using standard polishing techniques and a ⅓ HCl, ⅓ HNO_3, ⅓ acetic "mixed acid" etch. A typical light micrograph of the 309 GTA welds of alloy 1 is shown in Figure 5(a). Examination of the ferrite structure shows that the majority of the ferrite is of the skeletal morphology. This ferrite lies along the core of the solidified dendrites. In the lower center of the micrograph the ferrite outlines both the primary and secondary dendrite arms. In the upper portion of the micrograph wider regions of ferrite exist along the primary dendrite. This variation in width of the skeletal ferrite was common throughout the fusion zone; however, in general, the wide regions of ferrite were more common near the outer weld region.

Figure 5(b) shows a light micrograph of a weld in alloy 25-14 (see Table I). Welds in this alloy exhibited a lathy ferrite morphology. In this case, the ferrite laths are also confined within the solidification cell core. The origin of the ferrite morphologies shown in the micrographs of Figure 5 is clearly described by the schematics in Figure 3.

V. STEM ANALYSIS

Skeletal Ferrite. STEM analysis of welds containing the skeletal ferrite morphology were taken primarily from the 309 welds because of the desirable skeletal ferrite orientation obtained within the thin foils made for TEM and STEM studies. In a thicker weld, the probability of the columnar dendritic structure lying entirely within the plane of the foil is less. An advantage of having the dendritic structure within the plane of the foil is that it is much easier to distinguish skeletal ferrite from cellular or eutectic ferrite, which results from primary austenite solidification followed by the binary eutectic solidification along the line of two-fold saturation (Figure 3). With this orientation it is also

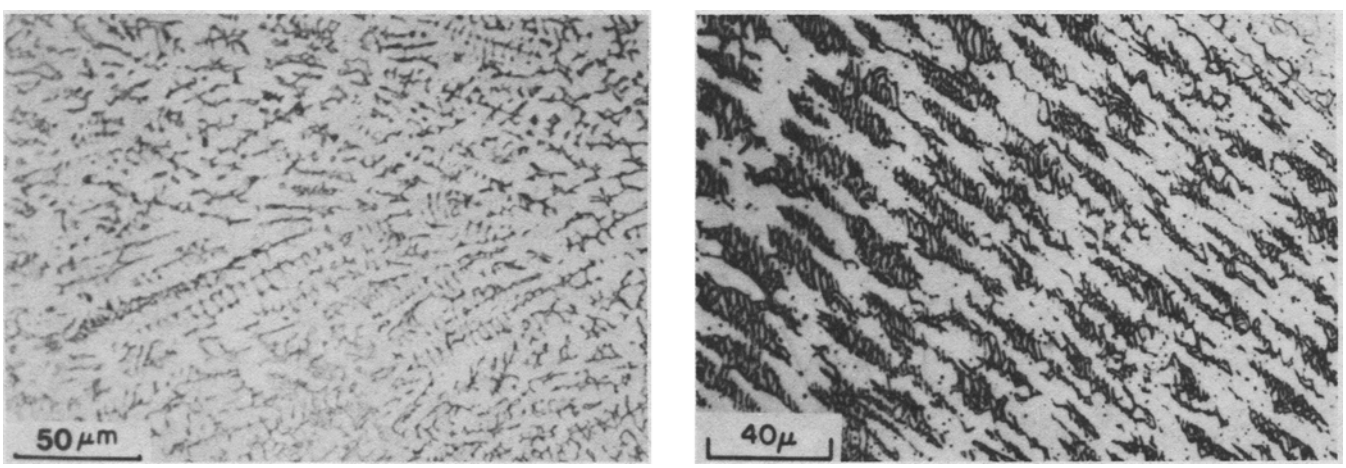

(*a*) (*b*)

Fig. 5—Light micrographs showing (*a*) skeletal ferrite in the 309 welds and (*b*) lathy ferrite in welds of alloy 25-14.

easier to distinguish between primary and secondary dendrite arms of the skeletal ferrite structure. This can be observed from the 309 weld structure of alloy #1 shown in the STEM image of Figure 6(a). Clearly shown is the skeletal ferrite along two primary dendrite arms in addition to well-defined secondary arms in one of the structures. The paths along which STEM analysis was conducted are shown in the STEM image of Figure 6(b); analyses were conducted between both primary and secondary arms. Figure 7(a) presents the Ni and Cr content of the ferrite and the composition profiles between two secondary arms. The Ni content of the austenite increases continually from the interphase boundary and reaches a maximum between the secondary arms. The Cr content of the austenite is maximum near the interphase boundary and decays to a uniform measured value of ~21.5 pct between the secondary arms.

Figure 7(b) shows the composition profiles obtained from STEM between the two primary arms taken across the region shown in Figure 6(b). Similar to the case of the secondary arms, the Cr content within the austenite between the primary arms is maximum near the interphase boundary but decreases to a rather uniform value within ~0.5 μm of the

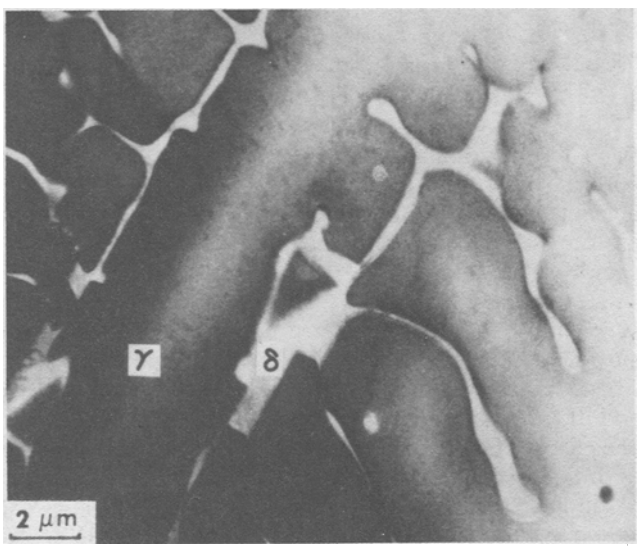

(*a*)

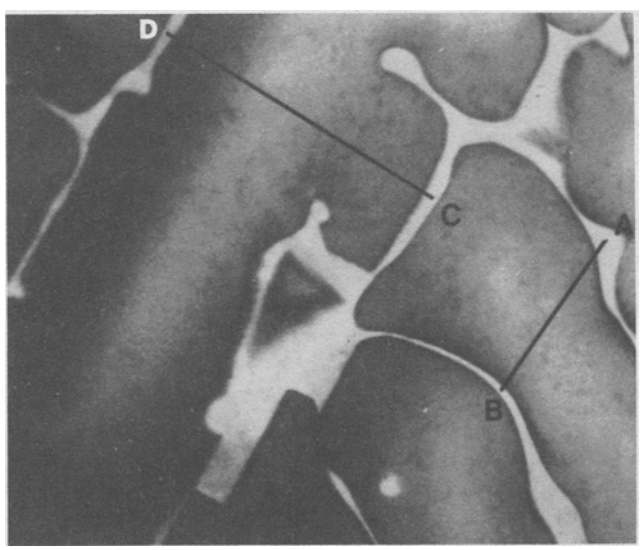

(*b*)

Fig. 6 — STEM images of a weld in the 309 alloy 1: (*a*) note apparent primary and secondary arms of skeletal ferrite, (*b*) regions of STEM analysis.

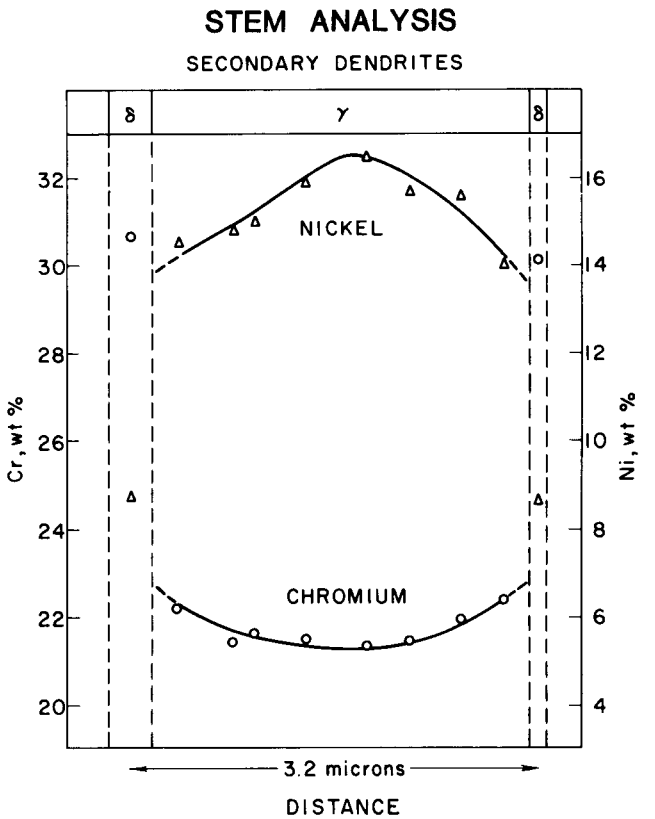

(*a*)

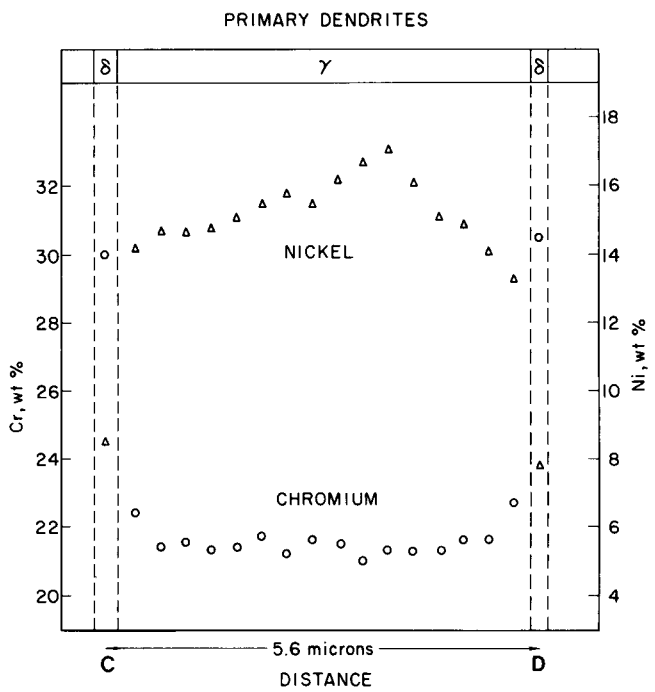

(*b*)

Fig. 7 — STEM analysis between the ferrite along secondary dendrite arms from A-B shown in Fig. 6(b), (*b*) STEM analysis between the ferrite along the primary dendrites, C-D in Fig. 6(b).

interphase boundaries. This uniform concentration continues across the cell boundary and again increases only within ~0.5 μm of the other interphase boundary.

The Ni concentration within the austenite between the two primary arms is skewed compared to that between the secondary arms due to the analysis extending between what appears to be two secondary arms of one of the primary dendrites. Following the path from C to D in Figure 7(b), the concentration of Ni is again minimum near the interphase boundary, fairly uniform between the secondary arms, and reaches a maximum in the cell boundary between the two primary arms. The Ni concentration extending from the primary dendrite at D may exhibit a slight plateau at ~15 pct before it reaches a maximum of ~17 pct near the cell boundary. A plateau may also exist just past where the secondary dendrite arms extend from C, also at ~15 pct Ni.

As shown in Figures 7(a) and (b), the ferrite is enriched in Cr and depleted in Ni with respect to the austenite. Detailed analysis was not conducted within the ferrite of this sample. It is also interesting to note that Fe, the third component of the system, is slightly enriched in the cell boundaries, between the ferrite compared to the austenite at the core nearest the ferrite.

Another weld ferrite morphology fairly common in some of the welds is a cellular-appearing ferrite network. STEM analysis was conducted in a partially cellular-ferrite-like region of a 309 weld from alloy #2. Two STEM images of the region analyzed are shown in Figure 8. Figure 8(a) is a low magnification micrograph showing some completed cells, which in this micrograph appear also to be associated with three primary dendrites. STEM analysis of the ferrite was conducted in the regions marked in Figures 8(a) and (b), and across the austenite from point 1 to point 24. The STEM analysis in the ferrite regions 1 and 24 and along the path within the austenite is shown in Figure 9. As can be seen, the ferrite in regions 1 and 24 contained measured values ~10 to 10.5 pct Ni and ~31.5 pct Cr. The Cr content within the austenite is fairly uniform at ~23.5 pct and increases only slightly very near the interphase boundary. The Ni content is characteristic of that of primary ferrite solidification: a maximum between the ferrite and a minimum near the interphase boundaries.[9,27,28] Note that both the amount of Ni partitioning and the Ni concentration profile are very similar to that between the two primary dendrites shown earlier (Figure 7(b)).

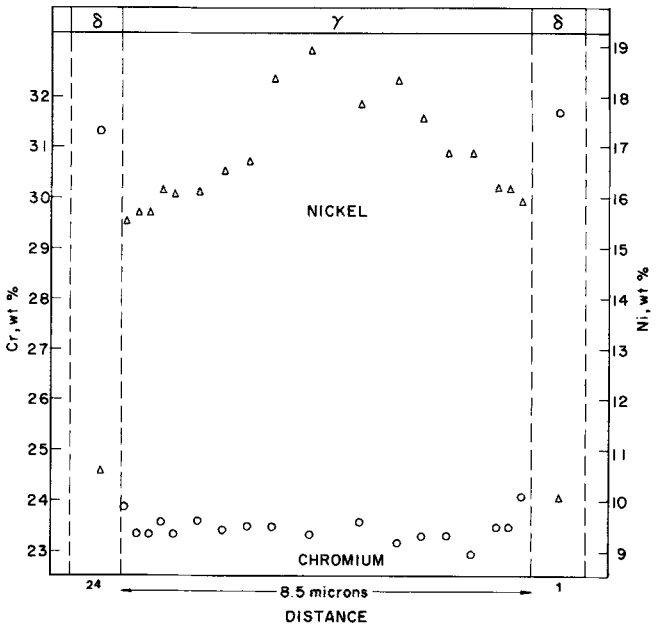

Fig. 9—STEM analysis of ferrite and austenite from regions 24-1 shown in Fig. 8.

The alloy compositions of the ferrite shown in Figure 8 were measured at the numbered points. The following results were obtained: (23) = 34.7 pct Cr and 7.6 pct Ni; (2) = 32.3 pct Cr and 10.5 pct Ni, and (25) = 30.3 pct Cr and 10.8 pct Ni. The error as represented by 2σ values of Cr and Ni are ~0.4 and 0.3 pct, respectively. The composition of different regions of the ferrite does vary, possibly due to partitioning upon cooling as discussed later. The somewhat skewed nature of the Ni profile within the austenite corresponds fairly well with the light region shown in the STEM image near the center of the cell in Figure 8(b). These high

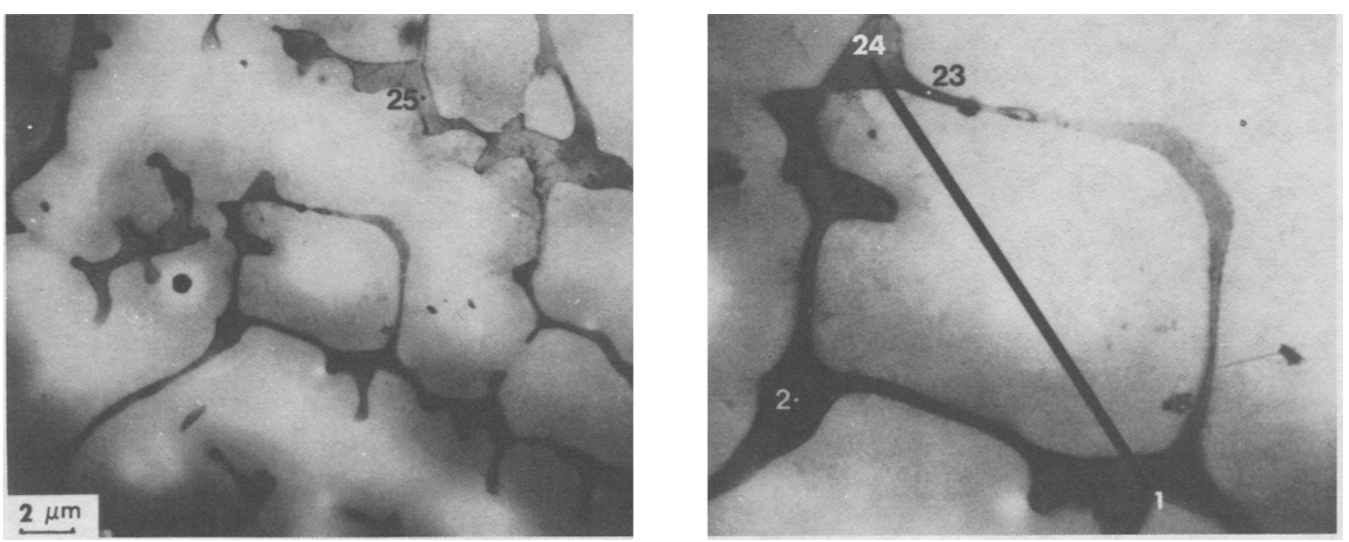

(a) (b)

Fig. 8—STEM images from a 309 weld in alloy 2 showing (*a*) skeletal ferrite and (*b*) a ferrite cell-like structure.

Ni regions of the austenite tend to thin preferentially during foil preparation as can also be seen from STEM images and analysis of Figures 6 and 7. Thus, the approximate concentration profiles can be predicted over a large region of the STEM micrograph shown in Figure 8. It appears that most of the ferrite formed as primary ferrite or at least has concentration profiles consistent with that mode of solidification.[9,27] This cellular-appearing ferrite structure has been described schematically by Suutala *et al.*[6]

Another region within the same 309 weld (alloy #1) foil as that shown in Figure 6 was STEM analyzed. A STEM micrograph is shown in Figure 10. The two ferrite-containing regions are again along the cell cores; however, the morphology is considerably different from that in Figure 6. The ferrite is much wider than that analyzed previously, and does not contain well-defined secondary arms. Also, at each end of the wider ferrite structures are partial loops or cells of ferrite. These cells are likely similar to that shown and analyzed in Figure 8, and found to result from primary ferrite solidification.

The regions analyzed in both the austenite and ferrite shown in Figure 10 were chosen where the phase boundary was of minimum width (*i.e.*, parallel to the beam). The contamination spots along regions analyzed are visible in the STEM micrograph. The STEM analysis within the austenite between points A and B is shown in Figure 11(a). As shown, the Ni content is maximum in the cell boundary between the two ferrite regions. The Ni concentration decays from a measured maximum of ~16.5 pct to a minimum of ~13.7 pct near the ferrite boundaries. The composition of Cr within the austenite is minimum, ~21 pct, within the cell boundary and slowly increases to ~22.5 pct near the interphase boundary. These data are quite similar to those between the two primary ferrite arms shown in Figure 7(b).

The STEM analysis within the ferrite is shown in Figure 11(b). Composition gradients also exist within the ferrite. However, the composition profiles are not nearly as symmetric about the center of the ferrite as in the case of the austenite. Ni increases from ~8 pct at one boundary (point C on Figure 10) to slightly over 9.5 pct within about 0.2 μm of the adjacent phase boundary (D), where it then decreases to somewhat less than 9 pct. The measured Cr content within the ferrite decreases from ~30.5 pct near the phase boundary C to ~28.2 pct near the other phase boundary D as shown in Figure 11. However, within ~0.2 μm of the boundary, the Cr concentration increases to slightly above ~29 pct.

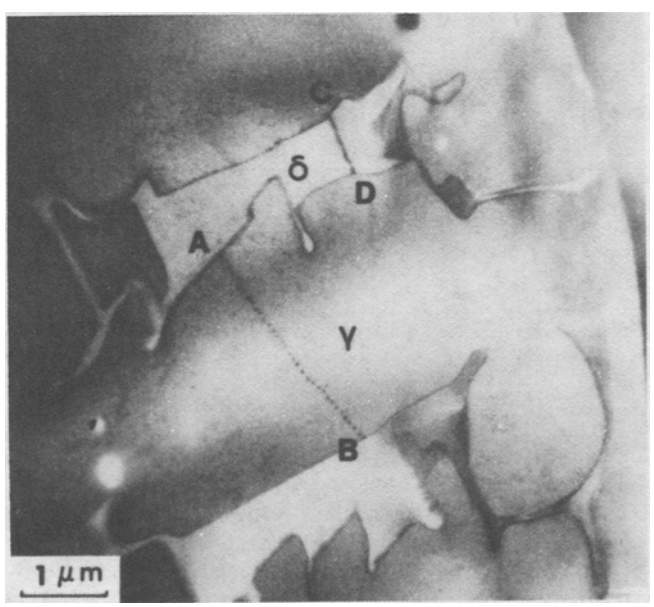

Fig. 10—STEM image showing regions of skeletal ferrite and austenite analyzed; contamination spots indicated regions analyzed—309 alloy 1.

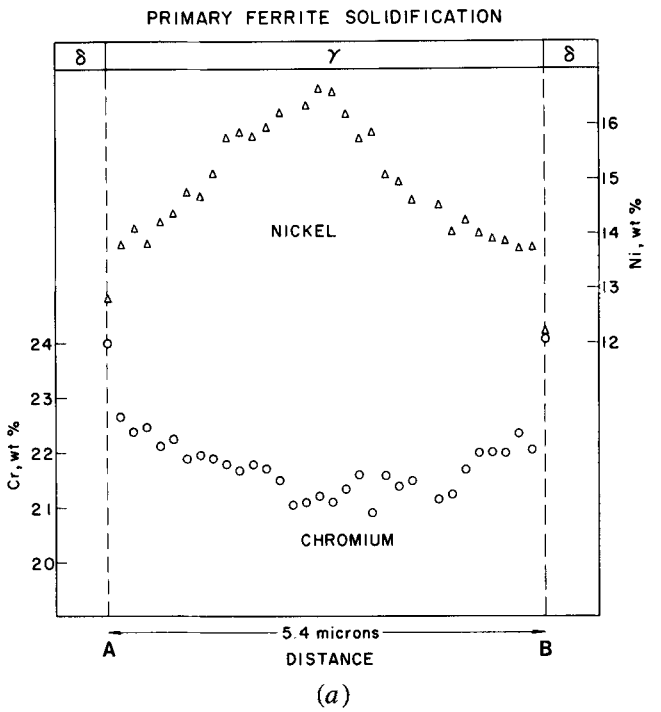

(*a*)

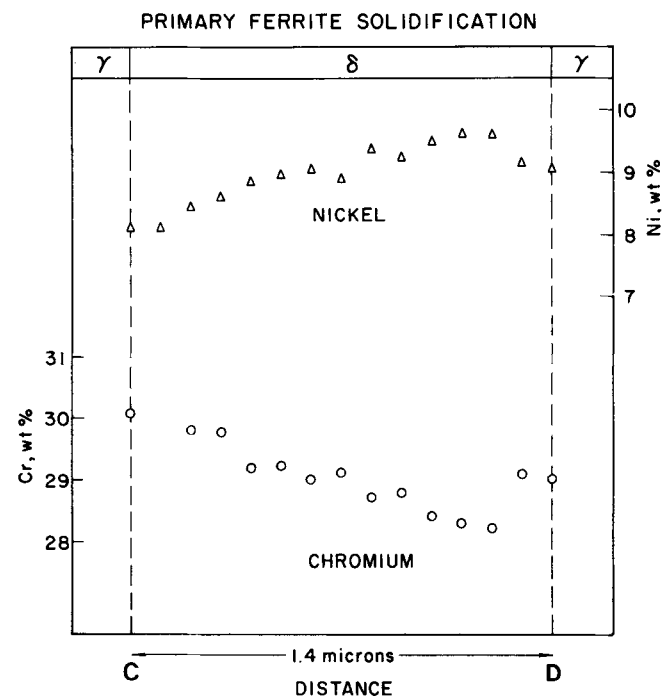

(*b*)

Fig. 11—(*a*) STEM analysis of austenite from A-B shown in Fig. 10. (*b*) STEM analysis of ferrite between C and D shown in Fig. 10.

Another STEM analysis was conducted on skeletal ferrite obtained from a small casting of alloy 22-13. The cooling rates were similar to those experienced in GTA welds, ~300 to 500 °C per second. Both the STEM image and STEM analysis are shown in Figure 12. The analysis was taken across the central core in a region where the boundaries were almost parallel to the viewing direction, as shown in (a). The analysis contained in (b) clearly shows that the Ni concentration is maximum at the center of the ferrite and reaches a minimum near the phase boundary. The variation in Cr content is opposite to that of Ni, *i.e.*, it is minimum within the ferrite center and maximum at the phase boundary. It should also be noted that the shapes of the concentration gradients within the ferrite cannot be due to some averaging of the two phases due to beam overlap, as can occur with tilted boundaries close to interfaces. If averaging had occurred, the gradients would be reversed.

Lathy Ferrite. Thin foils were taken also from the weld of alloy 25-14 exhibiting the lathy ferrite morphology shown in the light micrograph of Figure 5(b). The purpose of this paper is not to discuss the evolution of the lathy ferrite morphology. However, some data are presented to demonstrate the similarities of the alloy partitioning within this structure, and within the skeletal ferrite.

A STEM image of lathy ferrite is shown in Figure 13(a). Two ferrite laths are shown in the austenite matrix. It is agreed[6–10,19] that the ferrite in this structure is along the cell core, which solidified as ferrite, but partially transforms to austenite upon cooling. Some disagreement exists in the literature, however, as to whether in the lathy ferrite morphologies the austenite forms by a diffusionless,[7] or diffusion-controlled transformation.[10,20,29]

The STEM analysis taken across the region marked on the image of Figure 13(a) is shown in (b). A large difference in composition exists between the ferrite and austenite. The ferrite is more enriched in Cr and depleted in Ni than the austenite. Composition gradients of Ni and Cr exist in both the ferrite and austenite. Within the ferrite, Ni is maximum in the center of the lath and minimum near the interphase boundary; the opposite trend is seen for Cr. The measured difference in composition from the center of the ferrite lath near the interphase boundary is ~2 wt pct Ni and ~3 wt pct Cr.

The composition gradients are opposite in the austenite compared to the ferrite. Within the austenite, Ni is maximum at the center and decreases to a minimum near the interphase boundary. Cr is somewhat more uniform than Ni, but is a minimum at the center of the ferrite and is a maximum near the interphase boundary. Within the austenite, the Ni varied by ~1.5 wt pct from the center to the phase boundary while Cr varied by ~1 wt pct. The average composition of the austenite is ~15 pct Ni, 22 pct Cr, while that of ferrite is ~8 pct Ni, 31 pct Cr.

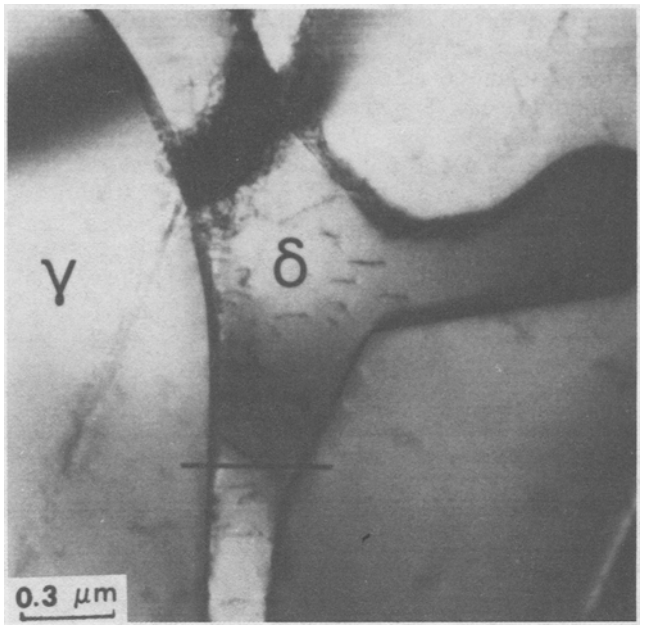

(*a*)

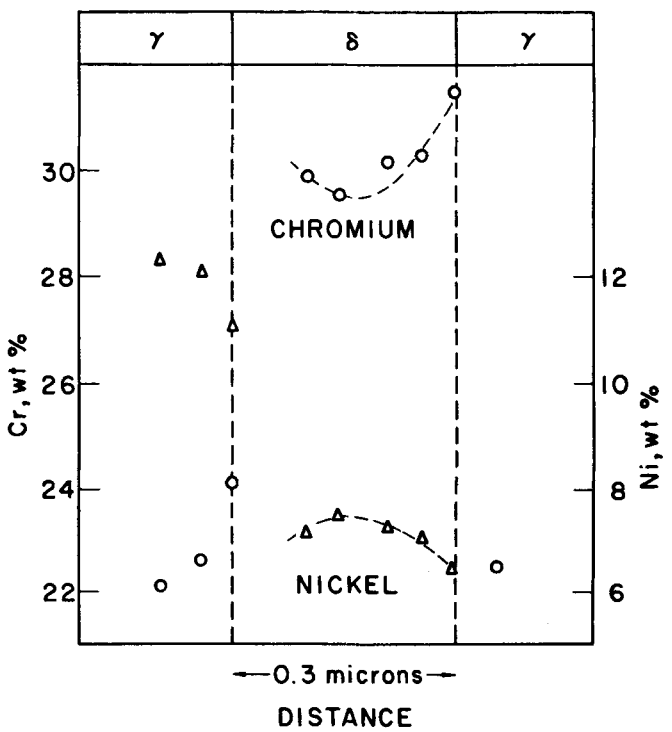

(*b*)

Fig. 12—STEM image (*a*) and analysis (*b*) of skeletal ferrite in a small casting of alloy 22-13.

VI. DISCUSSION

Skeletal Ferrite. The skeletal, or vermicular ferrite morphology studied here is probably the most commonly observed austenitic stainless steel weld microstructure. STEM data have been recently published in the literature on skeletal or vermicular-appearing ferrite morphologies. Detailed work was conducted by Lyman *et al*[28] on 304 welds. Although detailed analysis of microstructures was not shown, STEM images showed the structure to be skeletal in nature. Their measured concentration profiles are very similar to those shown in Figure 7 except for the lower alloy content of 304 welds *vs* 309 welds. STEM analysis conducted by David *et al*[20] on 308 weld metal also showed Cr and Ni concentration profiles near the ferrite-austenite boundaries to be similar to those in Figure 7.

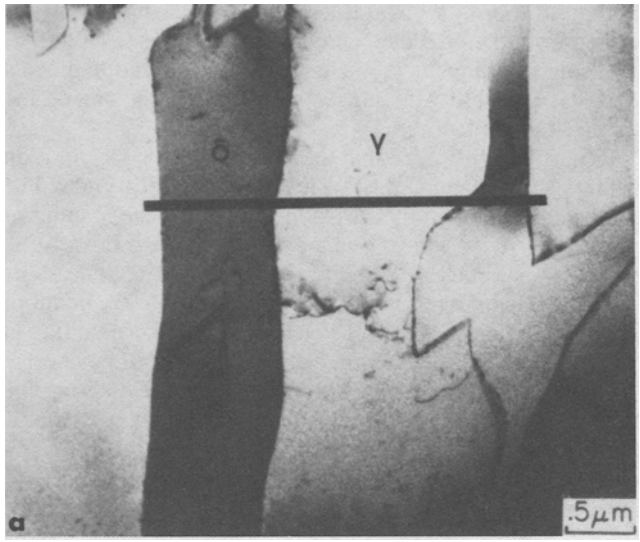

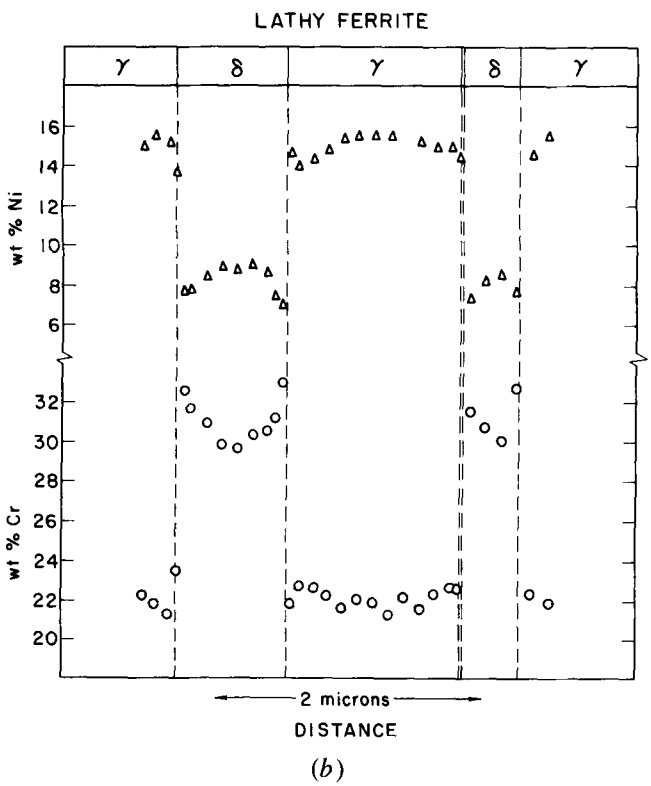

(*b*)

Fig. 13 — STEM image of lathy type ferrite shown in Fig. 4(b). Line indicates region of STEM analysis across the austenite and 2 ferrite laths shown in (*b*).

The STEM data on the structure shown in Figure 6 with primary and secondary arms can be compared with the rather wide ferrite regions of the structures shown in Figure 10. These two rather different ferrite morphologies were taken not only from the same 309 weld, but also the same thin foil. Therefore, the two regions were separated by only a small distance, on the order of 100 μm.

Lippold and Savage[17] used the STEM data of Lyman *et al*[28] to attempt to verify their solidification model (Figure 4), based on the equations of Tiller *et al*.[15] They concluded that diffusion times were too short to result in any significant diffusion, and thus they interpreted the measured concentration profiles and skeletal ferrite morphology, like those of Figure 7, to have resulted from the initial and final solidification transients, and a massive transformation of ferrite to austenite. Recently they have cited additional STEM data on 304 welds, which they conclude are also in agreement with this rationale.[18] However, they had to adjust their value of D_l to 2×10^{-6} cm^2 per second, rather than the more accepted values for diffusion in the liquid of $\sim 1 \times 10^{-5}$ cm^2 per second. Even though the welds they compared were made under different conditions by different investigators, in all cases the composition data were very similar. This seems to us to suggest that other common factors, such as diffusion, may be playing an important role. The length of the proposed initial transients were similar for both Cr and Ni and were ~0.1 to 0.2 μm.[18] This distance corresponds to the distance where the concentration of the initial transient decays to $1/e$.

The STEM profiles of the skeletal structure in Figure 6 can likewise be plotted in a manner to suggest an initial transient. However, as shown in Figure 7, no final transient is observed for Cr as would be predicted. A final Cr transient was also not observed in the work of Lyman *et al*.[28] The lengths of the initial and final transients would be expected to be similar in each case since the distribution coefficient k of both Cr and Ni is fairly close to one and the length of the final transient (for small k) is $\sim 1/k$ times the length of the initial transient. Conservation of solute requires either that the excess or depletion of solute within the initial transient region be accommodated within the final transient region.

The chemical concentration across the wide region of ferrite shown in Figure 10 can be seen in Figure 11 to be relatively uniform over a distance of ~1.4 μm compared to a sharp initial transient only a fraction of a micrometer in length. Also, the relatively high Cr and low Ni concentrations across this large region could not result by diffusion leveling of a short initial transient only 0.1 to 0.2 μm in length, since the concentration change due to the transient would be expected to decay to a value of $1/e$ over this short distance. These results showing relatively uniform, but high-Cr, low-Ni concentrations across the ferrite in the cell core are inconsistent with the rationale proposed by Lippold and Savage.[17,18]

The detailed STEM results presented in this study clearly show that considerable diffusion accompanies this transformation. The major difference between the wide ferrite structure shown in Figure 10 and the more skeletal-appearing structure in Figure 6 is most likely only the degree of partitioning which occurs during cooling. The maximum Cr and minimum Ni in each ferrite region is the same. The wider region of ferrite may have resulted from a slightly greater degree of primary ferrite solidification. If the cooling rate were slower the wide region of ferrite in Figure 10 would have been further consumed by austenite. This is consistent with the concept that slower cooling rates result in lower ferrite contents.

The nature of the concentration profiles within the ferrite shown in both Figures 11(b) and 12 are also consistent with solute partitioning. As the ferrite is consumed by the austenite upon cooling, Cr is rejected by the austenite while Ni is rejected from the ferrite, as predicted by the constant-Fe vertical sections. This results in an increased Cr content and decreased Ni content within the ferrite near the phase boundary, compared to the center of the ferrite structure. It is

interesting to note that the curvatures of the Cr and Ni concentration profiles of the skeletal ferrite in Figure 12 are opposite those predicted by an initial solidification transient and a diffusionless $\delta \rightarrow \gamma$ solid state transformation.

The variations of the ferrite composition of the structure shown in Figures 8 and 9 are likely due principally to different degrees of alloy partitioning during the solid state transformation. However, as can be seen from the data of Figures 11(b) and 12(b), some variations can also be expected to result from the exact location within the ferrite at which the analysis was taken. It should be pointed out that in all the regions of ferrite analyzed in the structure shown in Figure 8, the measured Fe concentration was constant at 58 pct. This is consistent with partitioning of only Cr and Ni within the ferrite and austenite during the solid state transformation.

It should also be noted that the composition profiles within the austenite of the cell core is consistent with alloy partitioning. As the ferrite is consumed by the austenite upon cooling, the solubility of Cr within the austenite increases and that of Ni decreases (see Figure 1). This will result in the Ni concentration decreasing toward the ferrite at the core and the Cr concentration increasing. This trend was observed in all the STEM data obtained from primary-ferrite-solidified welds. However, as can be seen by the STEM data, for example, in Figures 7 and 9, the Cr is often more uniform across the core and increases only within ~0.5 μm of the phase boundaries. This may be due to more diffusion leveling of Cr than Ni except at the final stages of the transformation. The diffusion coefficient of Cr is ~10 times that of Ni in austenite at these high temperatures.[22,23] The lower the temperature of the transformation, the less Cr leveling will be expected. This may be the case, for example, in the data shown in Figure 11(a). The wide region of ferrite in this structure is also consistent with a lower transformation temperature restricting the solid state transformation of $\delta \rightarrow \gamma$.

The above discussion is not meant to suggest that the overall composition profiles in skeletal ferrite structures result only from solute partitioning during the solid state transformation. The high Ni concentrations in the cell boundaries undoubtedly result from secondary austenite solidification due to Ni enrichment and Cr depletion of the liquid during primary ferrite solidification. From examination of the Ni concentration of Figures 7, 9, and 11, we suggest that the variation in Ni of the austenite of about the first 2 to 3 wt pct adjacent to the ferrite along the cell core is due mainly to partitioning during the solid state transformation, while the significantly higher concentration of Ni in the cell boundaries is a result only of segregation during solidification. The sometimes apparent change in the Ni concentration profile of the austenite may mark the onset of secondary austenite solidification. For example, a slight plateau appears to exist in the concentration profiles between the two primary arms at ~15.5 pct Ni shown in Figure 7(b). A similar region may also exist, for example, at ~3 μm from the δ-γ interface of the ferrite marked at "24" in Figure 9, and at the plateau ~1.5 μm from the skeletal ferrite toward the cell boundary in Figure 2 of Lyman's work.[28] We must point out that the conclusion of the onset of austenite solidification in these regions is somewhat speculative since migration of the ferrite-austenite interface during the solid state transformation eliminates any other physical evidence of the position of the solidification mode change. Also, as shown from the predicted composition profiles in Figure 2, a Ni solute "dump" is predicted by all solidification models with the possibility of no change in the structure of the solidifying solid.

It must be considered that the maximum Ni concentration within the cell boundaries as a result of solidification will be somewhat smoothed by diffusion. However, the amount of diffusion will be less if secondary austenite solidification results as opposed to 100 pct ferrite solidification, due to the higher diffusion rates in ferrite. Furthermore, the amount of partitioning during the solid state transformation resulting in concentration profiles within each phase will, of course, be dependent upon the composition of the ferrite entering the two phase region. Due to the shape of the solvus curves, more partitioning within each phase is expected for compositions closer to the eutectic trough; see Figure 1. Also, in this case, the time and temperatures are more favorable for diffusion.

Lathy Ferrite Structure. The STEM analysis, Figure 13(b), of the lathy ferrite morphology shown in Figures 5(b) and 13(a) clearly shows that this structure is also the product of a diffusion-controlled solid state transformation. Again, the composition profiles within both the ferrite and austenite are consistent with those resulting from the transformation of ferrite to austenite upon cooling through the two phase region. Partitioning can thus be explained in the same manner as above for the skeletal ferrite morphology. The composition profile within the lathy ferrite (Figure 13(b)) is very similar to that of the skeletal ferrite in Figure 12. It is further interesting to note that the Cr and Ni concentrations within the austenite of the lathy structure (Figure 13(b)) are very similar to those of the austenite within the core of the skeletal ferrite structure. This similarity in composition profiles between the skeletal and lathy ferrite morphologies is further evidence that the skeletal ferrite morphology is largely the product of a diffusion-controlled transformation. The transition from skeletal ferrite to lathy ferrite structures and the structures of the lathy ferrite morphologies were part of a larger study,[9] and are discussed elsewhere.[9,31]

Some discussion is warranted on the suggestion by Lippold and Savage[17] and Lyman *et al*[28] that diffusion distances are too great for diffusion to play a role in determining the final concentration profiles of the skeletal ferrite morphology. They estimate a diffusion distance $x \sim (4Dt)^{1/2}$ and identified the relevant x as the primary dendrite or cell spacings. This seems overly conservative with respect to the extent of diffusion required or the required diffusion distance. Distances between primary arms seem too large due both to the fact that only partial ferrite solidification occurs prior to the onset of secondary austenite solidification, and the much closer secondary than primary arm spacing for cellular dendritic solidification. For rapid solidification and cooling rates (1000 °C/sec^{-1} used[17] by Lippold and Savage, shorter times are available for diffusion; however, the resulting finer solidification structure also results in shorter required diffusion distances. Still of greater importance is the value used for the diffusion coefficient. Since the austenite is consuming the ferrite, diffusion must occur within the ferrite. The transformation kinetics are limited by diffusion of Cr and Ni.[30] The diffusion rates in ferrite are ~100 times greater[22,23] than the rates in austenite used by Lippold and Savage.[17]

VII. SUMMARY

STEM analysis was conducted on welds exhibiting a variety of skeletal ferrite morphologies and one lathy ferrite structure. The data show that the skeletal ferrite structure is a result of a diffusion-controlled solid state transformation during which a large fraction of the primary solidified ferrite transforms to austenite. During this transformation which occurs upon cooling, Cr partitions to the ferrite and Ni to the austenite; this fact explains the nature of the alloy composition profiles within each phase near the cell core. However, the maximum Ni concentrations along the solidification cell boundaries of the skeletal ferrite containing structure is likely the result of segregation during solidification rather than partition during the solid state transformation.

The lathy ferrite structure analyzed was also a product of a diffusion-controlled transformation. Alloy partitioning within this structure was very similar to that measured near the cell core of the skeletal ferrite-containing structures.

ACKNOWLEDGMENTS

This work was sponsored jointly by the Center for Joining of Materials — Carnegie-Mellon University and by the United States Department of Energy, DOE, under contract number DE-AC04-76DP00789.

REFERENCES

1. W. T. DeLong, G. A. Osram, and E. R. Szumachowski: *Welding J.*, 1965, vol. 35, pp. 521-s to 528-s.
2. G. M. Goodwin, N. C. Cole, and G. M. Slaughter: *Welding J.*, 1972, vol. 51, pp. 425-s to 429-s.
3. R. D. Thompson, Jr: in ASME Winter Conf. Proc., *Critical Materials and Fabrication Issues for Pressure Vessels, Piping, Pumps and Valves*, spons. by ASME and HBS, San Francisco, CA, December 10-15, 1978.
4. T. Tsuk, M. Hubert, and C. Messager: *Revue de Metallurgie*, December 1971, vol. 68, pp. 829-37.
5. F. C. Hull: *Welding J.*, 1967, vol. 46, pp. 399-s to 409-s.
6. N. Suutala, T. Takalo, and T. Moisio: *Metall. Trans. A*, 1979, vol. 10A, pp. 512-14.
7. J. C. Lippold and W. F. Savage: *Welding J.*, 1980, vol. 59, pp. 48-s to 58-s.
8. S. David: *Welding J.*, 1981, vol. 60, pp. 63-s to 71-s.
9. J. A. Brooks: Ph.D. Thesis, Carnegie-Mellon University, Pittsburgh, PA, April 1981.
10. H. Fredriksson: *Metall. Trans.*, 1972, vol. 3, pp. 2989-97.
11. G. J. Davies: *Solidification and Casting*, App. Sc. Pub. Ltd., 1973.
12. M. C. Flemings: *Solidification Processing*, McGraw-Hill, 1974.
13. J. Davies and J. G. Garland: *Inter. Met. Reviews*, 1975, vol. 20, pp. 83-105.
14. W. A. Tiller, K. A. Jackson, J. W. Rutter, and B. Chalmers: *Acta Met.*, 1953, vol. 1, p. 428.
15. V. G. Smith, W. A. Tiller, and J. W. Rutter: *Can. J. Phys.*, 1955, vol. 33, p. 733.
16. J. A. Burton, R. C. Prim, and W. P. Slichter: *J. Chem. Phys.*, 1953, vol. 21, p. 1987.
17. J. C. Lippold and W. F. Savage: *Welding J.*, 1979, vol. 58, pp. 362-s to 374-s.
18. J. C. Lippold and W. F. Savage: in *Modeling of Casting and Welding Processes*, H. Brody and D. Apelian, eds., TMS-AIME, Warrendale, PA, 1981, pp. 443-58.
19. Y. Arata, F. Matsuda, and S. Katayama: *Japanese Weld. Res. Inst. Trans.*, 1976, vol. 5(2), pp. 35-51.
20. S. A. David, G. M. Goodwin, and D. N. Braski: *Welding J.*, 1979, vol. 58, pp. 330-s to 336-s.
21. T. B. Massalski: in *Phase Transformations*, ASM, Metals Park, OH, 1970, pp. 433-86.
22. R. A. Perkins, R. A. Padgett, and N. K. Tunali: *Metall. Trans.*, 1973, vol. 4, pp. 2535-40.
23. R. A. Perkins: *Metall. Trans.*, 1973, vol. 4, pp. 1665-69.
24. Quantex-Ray Instruction Manual, KQNTX-1-80-2, KEVEX Corp.
25. G. Cliff and G. W. Lorimer: *Journal of Microscopy*, 1975, vol. 103, p. 203.
26. J. I. Goldstein: in *Introduction to Analytical Electron Microscopy*, J. Hren, J. Goldstein, and D. Joy, eds., Plenum Press, 1979, pp. 83-120.
27. J. A. Brooks, J. C. Williams, and A. W. Thompson: *Metall. Trans. A*, 1983, vol. 14A, pp. 75-84.
28. C. E. Lyman, P. E. Manning, D. J. Duquette, and E. Hull: *Scanning Electron Microscopy*, 1978, vol. 1, pp. 213-20.
29. N. Suutala, T. Takalo, and T. Moisio: *Metall. Trans. A*, 1979, vol. 10A, pp. 1183-90.
30. H. I. Aaronson, C. Laird, and K. R. Kinsman: in *Phase Transformations*, ASM, Metals Park, OH, 1970, pp. 313-93.
31. J. A. Brooks, J. C. Williams, and A. W. Thompson: Proceedings of *Trends in Welding Research in the United States*, S. A. David, ed., ASM, Metals Park, OH, 1982, pp. 331-55.